Photoionization of Xe and Xe@C_{60} from the 4*d* shell in RABBITT fields

Alexander W. Bray, Faiza Naseem, and Anatoli S. Kheifets
Research School of Physics and Engineering, The Australian National University, Canberra ACT 0200, Australia

(Received 27 August 2018; published 18 October 2018)

We consider photoemission from the 4*d* shell of the free Xe and encapsulated Xe@C_{60} atoms by ionizing XUV and probing IR fields typical for a RABBITT (reconstruction of attosecond beating by interference of two-photon transitions) measurement. Our theoretical model is based on the numerical solution of the time-dependent Schrödinger equation in the single-active-electron approximation. The fullerene C_{60} cage is represented by a finite-width well potential. We test our model against an analogous set of nonrelativistic [Phys. Rev. A **89**, 053424 (2014)] and relativistic [Phys. Rev. A **96**, 053407 (2017)] calculations for the 4*d* shell of Xe and Xe@C_{60} driven by a continuous XUV field. Based on this verification, we make predictions for the total ionization probability, angular anisotropy β parameter, and the angular-dependent atomic time delay τ_a from the threshold to several hundred eV of excess energy.

DOI: 10.1103/PhysRevA.98.043427

I. INTRODUCTION

The RABBITT (reconstruction of attosecond beating by interference of two-photon transitions) technique has been widely used to study the time-resolved dynamics of atomic [1–7] and molecular [8–10] photoemission. Recently, this technique has become angular resolved [11–13]. While the initial studies have been confined to a narrow photon energy range not exceeding 40 eV (24th harmonic of the fundamental radiation at $\lambda \simeq 800$ nm), the most recent experiments [7,14,15] extended this range above 100 eV. This has enabled the study of photoemission dynamics beyond the outer atomic shells and to probe the subvalent 4*d* shell of the Xe atom [14].

The photoemission dynamics of the 4*d* shell of Xe is rich. Right at the threshold, the $4d \to Ef$ photoionization channel is suppressed by the centrifugal barrier and the cross section is dominated by its $4d \to Ep$ counterpart. Away from the threshold, the $4d \to Ef$ channel displays a broad resonance centered below 100 eV of photon energy which completely dominates the cross section. This resonance originates from the outgoing photoelectron being trapped in a potential well made by the Coulomb field of the residual ion and the centrifugal potential. This so-called giant resonance [16] is so strong that it influences the photoemission dynamics of the outer valence $5p$ shell and changes considerably its partial photoionization cross section and the photoelectron angular anisotropy β parameter [17]. It also enhances the high-order harmonics spectrum generated in the Xe atom [18,19]. At higher photon energies approaching 200 eV, the f-wave dipole matrix element passes through a node and the photoionization cross section displays a Cooper minimum. In this photon energy range, the competition from the typically weak photoionization channel $4d \to Ep$ intensifies. This results in a strong variation of the photoelectron angular anisotropy relative to the polarization axis of light [20]. The photoemission dynamics of Xe becomes even richer inside a fullerene C_{60} cage. It exhibits multiple confinement resonances when the photoelectron de Broglie wavelength is comparable to the size of the cage [21,22].

Predictive theoretical modeling of a RABBITT measurement on a complex atom such as Xe would require an accurate solution of a multielectron time-dependent Schrödinger equation (TDSE) driven by the ionizing XUV and probing IR pulses. Such a solution in general cannot be found at present. However, when the intershell correlation is weak, the single-active-electron (SAE) approximation can be applied and the problem becomes numerically treatable. This is a typical situation for the outer valence subshells of noble-gas atoms [23]. The intershell correlation can also be neglected for the 4*d* shell of Xe at photon energies which do not approach the inner $4p$ shell threshold. In the present work we consider this region and apply our TDSE/SAE model for numerical simulations of RABBITT measurements on the 4*d* shell of the free Xe and encapsulated Xe@C_{60} atoms. Our calculation spans a wide photon energy range from the threshold to 200 eV excess energy and encompasses both the giant resonance and the Cooper minimum. We validate our TDSE/SAE model using the earlier calculations [24,25] which considered a photoemission process driven by a continuous XUV field. In contrast to Refs. [24,25], our present calculations can be compared directly with the RABBITT experiment without invocation of the so-called continuum-continuum (CC) [26] or Coulomb-laser coupling (CLC) [27] corrections.

The remainder of this paper is organized as follows. In Sec. II we describe our method and its numerical implementation. In Sec. III we outline and analyze our results. We conclude by highlighting links with existing experimental measurements and propose several new areas of interest.

II. THEORY

Solution of TDSE

As previously [23,28], we solve the one-electron TDSE written in the SAE as

$$i\partial\Psi(\boldsymbol{r})/\partial t = [\hat{H}_{\rm atom} + \hat{H}_{\rm int}(t)]\Psi(\boldsymbol{r}). \quad (1)$$

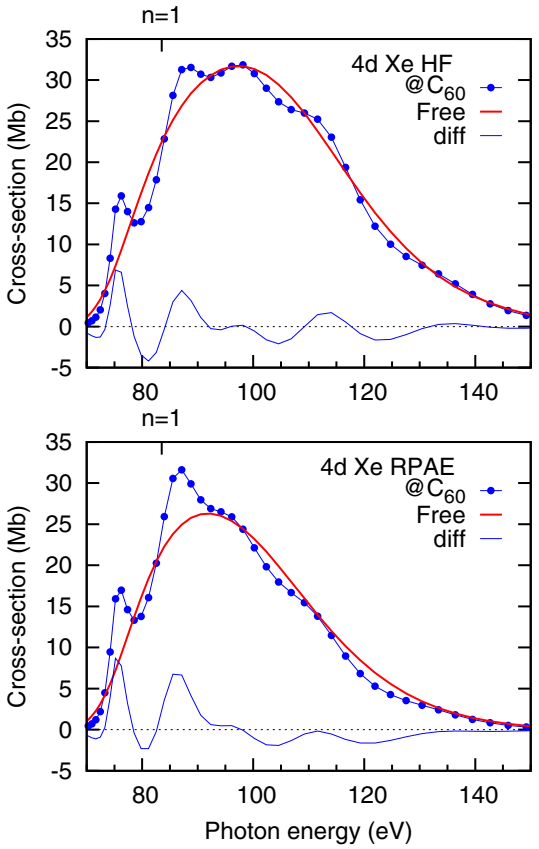

FIG. 1. The angular integrated $\sigma_{4d\to Ef}$ photoionization cross section of the free Xe (solid red line) and encapsulated Xe@C_{60} (dotted blue line) atoms calculated in the HF (top) and RPAE (bottom) models. The difference of the Xe@C_{60} and Xe cross sections is highlighted by the thin blue solid line.

The electromagnetic interaction is chosen in the velocity gauge

$$\hat{H}_{\rm int}(t) = \boldsymbol{A}(t)\cdot\hat{\boldsymbol{p}}, \quad \boldsymbol{A}(t) = -\int_0^t \boldsymbol{E}(t')dt'. \tag{2}$$

This interaction includes both the XUV and IR fields. The XUV field is modeled by an attosecond pulse train (APT) with the vector potential

$$A_x(t) = \sum_{n=-5}^{5}(-1)^n A_n \exp\left(-2\ln 2\frac{(t-nT/2)^2}{\tau_x^2}\right) \times \cos\left[\omega_x(t-nT/2)\right], \tag{3}$$

where $A_n = A_0\exp\left(-2\ln 2\frac{(nT/2)^2}{\tau_T^2}\right)$. Here, A_0 is the vector potential peak value and $T = 2\pi/\omega$ is the period of the IR field. The XUV central frequency is ω_x and the time constants τ_x, τ_T are chosen to span a sufficient number of harmonics in the range of photon frequencies of interest.

The vector potential of the IR pulse is modeled by the cosine squared envelope

$$A(t) = A_0\cos^2\left(\frac{\pi(t-\tau)}{2\tau_{\rm IR}}\right)\cos[\omega(t-\tau)]. \tag{4}$$

The IR pulse is shifted relative to the APT by a variable delay τ such that the RABBITT signal of an even $2q$ sideband (SB) oscillates as

$$S_{2q}(\tau) = A + B\cos[2\omega\tau - C]. \tag{5}$$

The solution of the TDSE (1) is found using the iSURF method as given in Ref. [29].

The choice of the one-electron potential entering Eq. (1) is described in Ref. [23]. As in Ref. [24], an attractive spherical square well potential is introduced to represent the C_{60} cage,

$$V(r) = \begin{cases} -U_0 < 0 & \text{if } R_{\rm inner} \leqslant r \leqslant R_{\rm inner}+\Delta, \\ 0 & \text{otherwise.} \end{cases} \tag{6}$$

Here, $R_{\rm inner} = 5.8$ a.u., $\Delta = 1.9$ a.u., and $U_0 = 0.302$ au. Such a simple model is adequate in the present case because the $4d$ subshell is sufficiently deeply bound and cannot hybridize with any of the levels of C_{60}. In addition, the photon energy range (80–200 eV) is well away from the C_{60} plasmons so that interchannel coupling with atomic photoionization is not important.

The RABBITT parameters A, B, and C entering Eq. (5) can be expressed as

$$A = |\mathcal{M}_{\boldsymbol{k}}^{(-)}|^2 + |\mathcal{M}_{\boldsymbol{k}}^{*(+)}|^2, \quad B = 2\,{\rm Re}[\mathcal{M}_{\boldsymbol{k}}^{(-)}\mathcal{M}_{\boldsymbol{k}}^{*(+)}],$$
$$C = \arg[M_{\boldsymbol{k}}^{(-)}M_{\boldsymbol{k}}^{*(+)}] = 2\omega\tau_a. \tag{7}$$

Here, $\mathcal{M}_{\boldsymbol{k}}^{(\pm)}$ are complex amplitudes for the angle-resolved photoelectron momentum $\boldsymbol{k}$ produced by adding or subtracting an IR photon, respectively. By adopting the soft photon approximation (SPA) [30] we can write

$$A, B \propto |J_1(\boldsymbol{\alpha}_0\cdot\boldsymbol{k})|^2|\langle f|z|i\rangle|^2 \propto [1+\beta P_2(\cos\theta_k)]\cos^2\theta_k. \tag{8}$$

Here, β is the angular anisotropy parameter, J_1 is the first-kind Bessel function of the order 1, P_2 is the second-order Legendre polynomial, $\boldsymbol{\alpha}_0 = \boldsymbol{E}_0/\omega^2$, $\langle f|z|i\rangle$ is the dipole matrix element, and θ_k is the emission angle relative to the joint polarization axis of the XUV and IR pulses (see the Appendix of Ref. [23] for the derivation). The C parameter is converted to the atomic time delay τ_a by (7) and analyzed as a function of the photoelectron direction relative to the polarization axis. The angular dependence of τ_a is compared with the analogous dependence of the Wigner time delay $\tau_{\rm W}$ [25] augmented by the CC correction $\tau_{\rm CC}$ [26].

III. RESULTS

A. Integrated photoionization cross sections

In this section, we first verify that the SAE is adequate to describe the photoionization of the $4d$ subshell of the free and encapsulated Xe atoms and the correlation with outer atomic shells can be neglected. We do so by performing the two sets of calculations using a noncorrelated Hartree-Fock (HF) model and the fully correlated random-phase approximation with exchange (RPAE). The latter is known to describe adequately both the valent and subvalent shell photoionizations of noble-gas atoms by continuous XUV fields [17]. Results of these calculations are shown in Fig. 1.

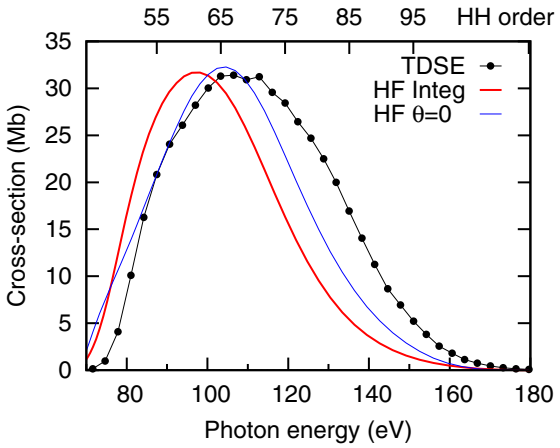

FIG. 2. The normalized intensity of the HH peaks in the photoelectron spectrum (dotted line) is compared with the angular integrated photoionization cross section $\sigma_{4d\to Ef}$ (thick red solid line) and the same cross section in the forward direction $\sigma_{4d\to Ef} \times [1 + \beta(E)]$ (thin blue solid line).

We find that the angular integrated $\sigma_{4d\to Ef}$ photoionization cross sections from the HF and RPAE calculations are qualitatively very close. Moreover, the variation of the cross section due to the C_{60} cage is very similar in both calculations. The largest variation occurs near the first confinement resonance $n = 1$ when the photoelectron de Broglie wavelength scales with the cage radius $n\lambda = 2\pi n/k = R$. Here, k is the photoelectron momentum $k^2/2 = \omega - I_p$ from the photon of energy ω above the ionization potential I_p.

The photoionization cross section can also be deduced from the TDSE calculation. In Fig. 2 we show the intensity of the odd peaks in the photoelectron spectrum normalized to the high-order harmonics (HH) intensity in the APT spectrum. The odd HH data points are connected by lines to guide the eye. In the same figure, we also plot the angular integrated photoionization cross section $\sigma_{4d\to Ef}$ in the HF approximation and the same cross section in the light polarization direction $\sigma_{4d\to Ef} \times [1 + \beta(E)]$. All the cross sections are normalized to the $\sigma_{4d\to Ef}$ at its maximum. We see that there is a close correspondence of all the three sets of cross sections that display a profound maximum (giant resonance) near 100-eV photon energy. The HF cross section amended by the β factor is closer to the TDSE result as the HHG process is confined to the polarization direction.

B. Angular anisotropy β parameters

As was shown previously [23], the angular anisotropy β parameters can be deduced from the angular variation of the A and B parameters Eq. (7), and additionally from an analogous variation of the HH peaks in the photoelectron spectrum, through its proportionality to the conventional angular factor $1 + \beta(E)P_2(\cos\theta_k)$. The three sets of β parameters marked as HH, A, and B are displayed on the bottom panel of Fig. 3. As before, the HH data points are presented in a connected fashion to guide the eye. The calculations for the free Xe and encapsulated Xe@C_{60} atoms are shown along with their difference. The corresponding sets of β parameters from the

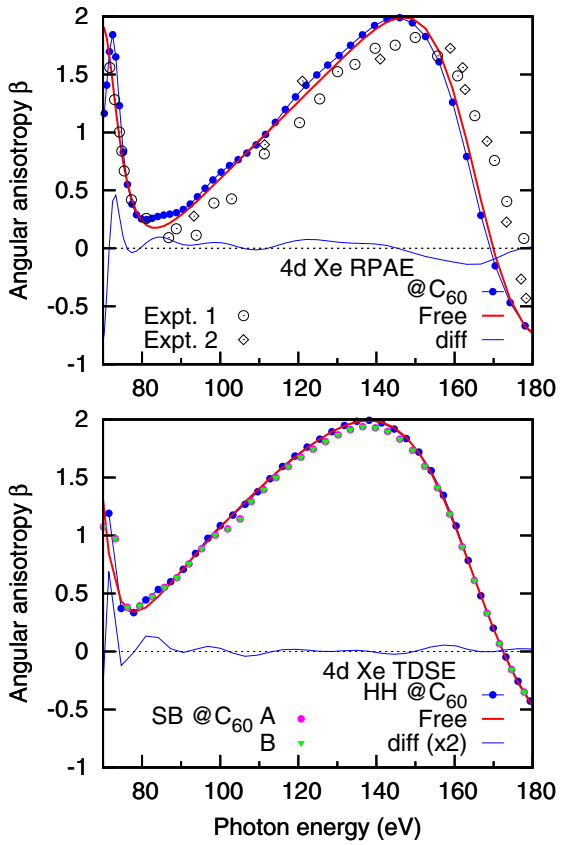

FIG. 3. Angular anisotropy β parameters of the $4d$ subshell of Xe from the RPAE (top) and TDSE (bottom) calculations. The dotted line visualizes the encapsulated Xe@C_{60} atom whereas the solid red line displays the free Xe atom. The difference of the Xe@C_{60} and Xe results is highlighted by a thin blue solid line. The three sets of the β parameters in the TDSE are deduced from the angular variation of the high-order harmonic peaks (HH) as well as the A and B parameters Eq. (7). The cage-free experimental data collated in Ref. [31] are shown with open circles and diamonds (top panel).

XUV-only RPAE calculation are displayed on the top panel of this figure. The two sets of experimental data collated in Ref. [31] are shown with open circles and diamonds. Both figures show close sets of β parameters with a fair correspondence between the RPAE and TDSE results as well as all the three sets of the HH, A, and B parameters. The β oscillations with the photon energy in the confined Xe@C_{60} atom are similar but somewhat dampened in the TDSE calculation as compared to the RPAE. The progressive deviation of the RPAE calculation from the experiment visible on the top panel of Fig. 3 indicates an onset of the $4d/4p$ intershell correlation which is not included in the present calculation. This agreement can be significantly improved in a fully relativistic RRPA calculation with inclusion of all interacting subshells [22].

C. Time delay

The atomic time delay in the polarization direction is shown in Fig. 4. On the top panel we show the RPAE result which we express as the sum $\tau_a = \tau_W + \tau_{cc}$ of the Wigner time delay and the regularized CC correction displayed in

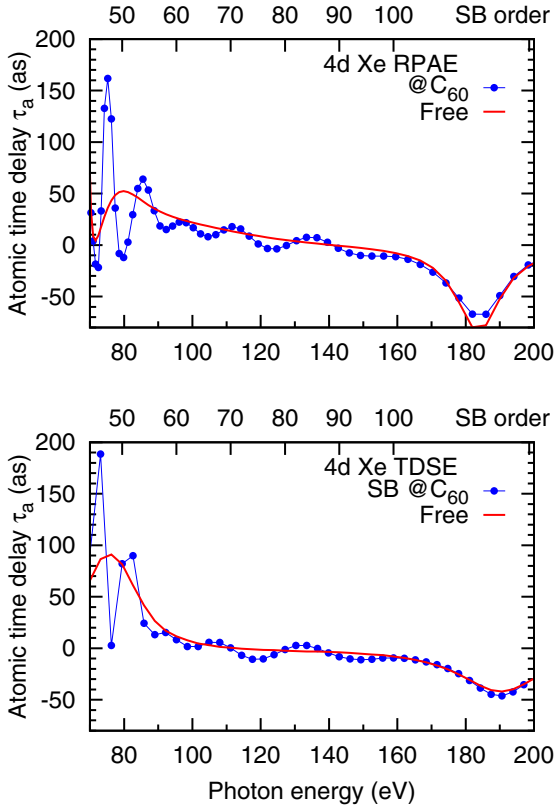

FIG. 4. Atomic time delay τ_a in the polarization direction deduced from the RPAE calculation as the sum $\tau_W + \tau_{cc}$ (top) and as obtained directly from TDSE by Eq. (7) (bottom). The dotted blue line visualizes the Xe@C_{60} calculation whereas the solid red line shows the free Xe atom result.

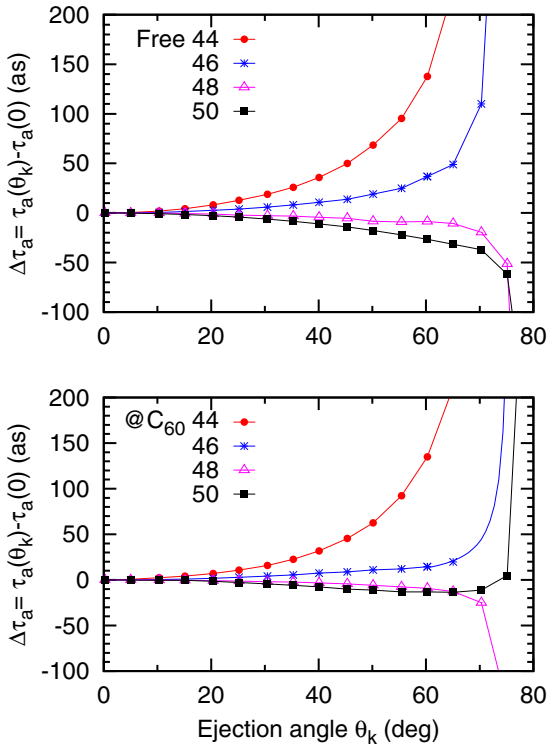

FIG. 5. Angular variation of the atomic time delay $\Delta\tau_a = \tau_a(\theta_k) - \tau_a(0)$ with the photoelectron emission direction for various sidebands. Top: the free Xe atom. Bottom: the trapped Xe@C_{60} atom.

Fig. 7 of Ref. [26]. The Wigner time delay is calculated as the energy derivative of the $4d$ photoionization amplitude [32]. On the bottom panel we show the TDSE result calculated directly using Eq. (7). In this figure, and in those following, the TDSE results are presented as connected to guide the eye. We see that both sets of calculations show a close correspondence, both for the free and encapsulated Xe atoms. The largest oscillation of the time delay occurs at the same photon energy range as of the β parameter and the angular integrated cross section and corresponds to the de Broglie wavelength resonating with the fullerene cage.

The angular variation of the atomic time delay $\Delta\tau_a = \tau_a(\theta_k) - \tau_a(0)$ is displayed in Fig. 5 for the free (top) and encapsulated (bottom) Xe atoms. In this figure we selected the sidebands where the energy oscillation of the time delay shown in Fig. 4 is largest. We see that the angular variation changes significantly with an increase of the SB order. This change is somewhat larger in the free Xe atom with a significant negative variation in SB48 and 50. This effect is less prominent in the Xe@C_{60} atom where, with the exception of SB44, there is only a significant angular variation beyond the 70° emission angle.

At higher photon energies, the $4d \rightarrow Ef$ photoionization channel dominates completely and the angular variation of the time delay vanishes. Another area of a significant angular variation of the time delay is near the Cooper minimum above the photon energy of 180 eV. This angular variation is shown in Fig. 6. Here, the angular variation is always positive and the time delay grows with increasing photoelectron emission angle. This growth begins immediately with the angular increase in contrast to the near-threshold region shown in Fig. 5. It is attributed to the weakening of the typically stronger $4d \rightarrow Ef$ photoemission channel and a more intense competition from its normally minor partner $4d \rightarrow Ep$. The effect of trapping is minimal at the photoelectron energy as the de Broglie wavelength is much smaller than the cage radius.

IV. CONCLUSIONS

We carried out a systematic investigation of the photoionization parameters that can be extracted from an angular-resolved RABBITT measurement on the $4d$ shell of the Xe atom and compared them with their analogs obtained in a typical continuous-wave synchrotron experiment. We analyzed the angular integrated photoionization cross section σ, the angular anisotropy β parameter, and the atomic time delay τ_a. The latter is studied along the polarization direction as well as a function of the photoelectron emission angle. The XUV+IR RABBITT simulations and the XUV-only continuous-wave calculations are carried out both on free Xe and trapped Xe@C_{60} atoms. The effect of the cage is found to be strongest when the photoelectron de Broglie wavelength $\lambda = 2\pi/k$ is close to the cage radius R. For the RABBITT simulations, we solved the time-dependent Schrödinger equation in the single-active-electron approximation. For

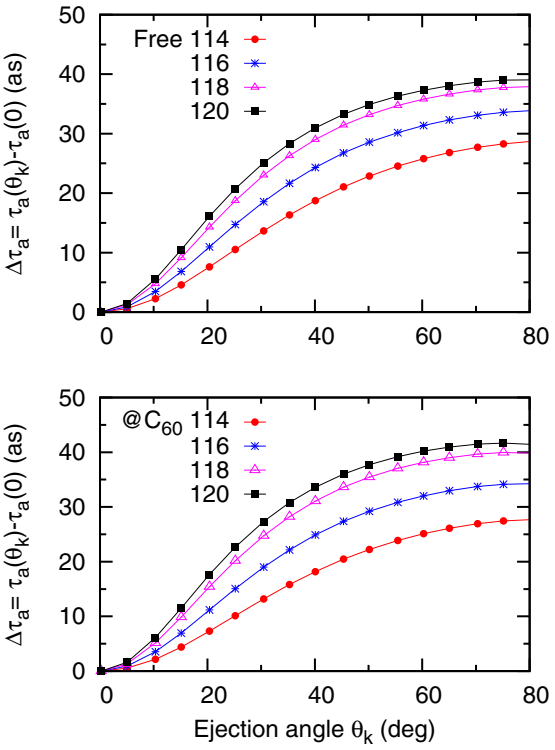

FIG. 6. Same as in Fig. 5 near the Cooper minimum.

XUV-only simulations, we additionally employed the random-phase approximation with exchange. In both cases, the C_{60} cage was modeled by a simple well potential.

The σ and β parameters from the XUV+IR and XUV-only simulations are generally quite close. This indicates that the RABBITT technique is fully compatible with the large body of earlier synchrotron measurements. In addition, RABBITT is capable of accessing the atomic time delay and subsequently the phase of the photoemission amplitude. This phase is otherwise difficult to characterize.

In the present study, we assumed that the probing IR field is weak and neglected the effect of the C_{60} cage polarization. In future developments, we will consider this effect along the lines suggested in Ref. [33].

We hope that the present work will guide the new generation of RABBITT measurements accessing very large sideband orders and deeper atomic shells. These measurements have been reported in the literature very recently [7,14,15]. In heavier atoms and deeper atomic shells such as Xe $4d$, the spin-orbit splitting effects become noticeable. In the present implementation of the TDSE code, this splitting can be mimicked by adjusting the one-electron potential to match the experimental $4d_{3/2}$ and $4d_{5/2}$ thresholds [14]. A more appropriate treatment would include a relativistic extension of the TDSE code. This work is now underway.

ACKNOWLEDGMENTS

The authors enjoyed many useful interactions with Thomas Gaumnitz. They are also thankful to Serguei Patchkovskii who placed his iSURF TDSE code at their disposal. Resources of the National Computational Infrastructure facility were employed.

[1] M. Swoboda, T. Fordell, K. Klünder, J. M. Dahlström, M. Miranda, C. Buth, K. J. Schafer, J. Mauritsson, A. L'Huillier, and M. Gisselbrecht, Phase Measurement of Resonant Two-Photon Ionization in Helium, Phys. Rev. Lett. **104**, 103003 (2010).

[2] K. Klünder, J. M. Dahlström, M. Gisselbrecht, T. Fordell, M. Swoboda, D. Guénot, P. Johnsson, J. Caillat, J. Mauritsson, A. Maquet, R. Taïeb, and A. L'Huillier, Probing Single-Photon Ionization on the Attosecond Time Scale, Phys. Rev. Lett. **106**, 143002 (2011).

[3] D. Guénot, K. Klünder, C. L. Arnold, D. Kroon, J. M. Dahlström, M. Miranda, T. Fordell, M. Gisselbrecht, P. Johnsson, J. Mauritsson *et al.*, Photoemission-time-delay measurements and calculations close to the 3s-ionization-cross-section minimum in Ar, Phys. Rev. A **85**, 053424 (2012).

[4] D. Guénot, D. Kroon, E. Balogh, E. W. Larsen, M. Kotur, M. Miranda, T. Fordell, P. Johnsson, J. Mauritsson, M. Gisselbrecht *et al.*, Measurements of relative photoemission time delays in noble gas atoms, J. Phys. B **47**, 245602 (2014).

[5] C. Palatchi, J. M. Dahlström, A. S. Kheifets, I. A. Ivanov, D. M. Canaday, P. Agostini, and L. F. DiMauro, Atomic delay in helium, neon, argon and krypton, J. Phys. B **47**, 245003 (2014).

[6] I. Jordan, M. Huppert, S. Pabst, A. S. Kheifets, D. Baykusheva, and H. J. Wörner, Spin-orbit delays in photoemission, Phys. Rev. A **95**, 013404 (2017).

[7] M. Isinger, R. Squibb, D. Busto, S. Zhong, A. Harth, D. Kroon, S. Nandi, C. L. Arnold, M. Miranda, J. M. Dahlström *et al.*, Photoionization in the time and frequency domain, Science **358**, 893 (2017).

[8] S. Haessler, B. Fabre, J. Higuet, J. Caillat, T. Ruchon, P. Breger, B. Carré, E. Constant, A. Maquet, E. Mével *et al.*, Phase-resolved attosecond near-threshold photoionization of molecular nitrogen, Phys. Rev. A **80**, 011404 (2009).

[9] J. Caillat, A. Maquet, S. Haessler, B. Fabre, T. Ruchon, P. Salières, Y. Mairesse, and R. Taïeb, Attosecond Resolved Electron Release in Two-Color Near-Threshold Photoionization of N_2, Phys. Rev. Lett. **106**, 093002 (2011).

[10] M. Huppert, I. Jordan, D. Baykusheva, A. von Conta, and H. J. Wörner, Attosecond Delays in Molecular Photoionization, Phys. Rev. Lett. **117**, 093001 (2016).

[11] S. Heuser, A. Jiménez Galán, C. Cirelli, C. Marante, M. Sabbar, R. Boge, M. Lucchini, L. Gallmann, I. Ivanov, A. S. Kheifets *et al.*, Angular dependence of photoemission time delay in helium, Phys. Rev. A **94**, 063409 (2016).

[12] J. Vos, L. Cattaneo, S. Patchkovskii, T. Zimmermann, C. Cirelli, M. Lucchini, A. Kheifets, A. S. Landsman, and U. Keller, Orientation-dependent stereo Wigner time delay in a small molecule, Science **360**, 1326 (2018).

[13] C. Cirelli, C. Marante, S. Heuser, C. L. M. Petersson, A. J. Galán, L. Argenti, S. Zhong, D. Busto, M. Isinger, S. Nandi *et al.*, Anisotropic photoemission time delays close to a Fano resonance, Nat. Commun. **9**, 955 (2018).

[14] A. Jain, T. Gaumnitz, A. W. Bray, A. S. Kheifets, and H. J. Wörner, Photoionization delays in xenon using single-shot referencing in the collinear back-focusing geometry, Opt. Lett. **43**, 4510 (2018).

[15] A. Jain, T. Gaumnitz, A. S. Kheifets, and H. J. Wörner, Using a passively stable attosecond beamline for relative photoemission time delays at high XUV photon energies, Optics Expr. **26** (2018).

[16] *Giant Resonance in Atoms, Molecules and Solids*, edited by J. P. Connerade, J. E. Esteva, and R. Karnatak, NATO ASI Series B Vol. 151 (Plenum, New York, 1986).

[17] M. Y. Amusia, *Atomic Photoeffect* (Plenum, New York, 1990).

[18] A. D. Shiner, B. E. Schmidt, C. Trallero-Herrero, H. J. Worner, S. Patchkovskii, P. B. Corkum, J. C. Kieffer, F. Legare, and D. M. Villeneuve, Probing collective multi-electron dynamics in xenon with high-harmonic spectroscopy, Nat. Phys. **7**, 464 (2011).

[19] D. Faccialà, S. Pabst, B. D. Bruner, A. G. Ciriolo, S. De Silvestri, M. Devetta, M. Negro, H. Soifer, S. Stagira, N. Dudovich *et al.*, Probe of Multielectron Dynamics in Xenon by Caustics in High-Order Harmonic Generation, Phys. Rev. Lett. **117**, 093902 (2016).

[20] D. W. Lindle, T. A. Ferrett, P. A. Heimann, and D. A. Shirley, Photoemission from Xe in the vicinity of the 4*d* Cooper minimum, Phys. Rev. A **37**, 3808 (1988).

[21] A. L. D. Kilcoyne, A. Aguilar, A. Müller, S. Schippers, C. Cisneros, G. Alna'Washi, N. B. Aryal, K. K. Baral, D. A. Esteves, C. M. Thomas *et al.*, Confinement Resonances in Photoionization of Xe@C_{60}^{+}, Phys. Rev. Lett. **105**, 213001 (2010).

[22] R. A. Phaneuf, A. L. D. Kilcoyne, N. B. Aryal, K. K. Baral, D. A. Esteves-Macaluso, C. M. Thomas, J. Hellhund, R. Lomsadze, T. W. Gorczyca, C. P. Ballance *et al.*, Probing confinement resonances by photoionizing Xe inside a C_{60}^{+} molecular cage, Phys. Rev. A **88**, 053402 (2013).

[23] A. W. Bray, F. Naseem, and A. S. Kheifets, Simulation of angular-resolved RABBITT measurements in noble-gas atoms, Phys. Rev. A **97**, 063404 (2018).

[24] P. C. Deshmukh, A. Mandal, S. Saha, A. S. Kheifets, V. K. Dolmatov, and S. T. Manson, Attosecond time delay in the photoionization of endohedral atoms A@C_{60}: A probe of confinement resonances, Phys. Rev. A **89**, 053424 (2014).

[25] A. Mandal, P. C. Deshmukh, A. S. Kheifets, V. K. Dolmatov, and S. T. Manson, Angle-resolved wigner time delay in atomic photoionization: The 4*d* subshell of free and confined Xe, Phys. Rev. A **96**, 053407 (2017).

[26] J. Dahlström, D. Guénot, K. Klünder, M. Gisselbrecht, J. Mauritsson, A. L. Huillier, A. Maquet, and R. Taïeb, Theory of attosecond delays in laser-assisted photoionization, Chem. Phys. **414**, 53 (2012).

[27] S. Nagele, R. Pazourek, J. Feist, K. Doblhoff-Dier, C. Lemell, K. Tőkési, and J. Burgdörfer, Time-resolved photoemission by attosecond streaking: extraction of time information, J. Phys. B **44**, 081001 (2011).

[28] I. A. Ivanov and A. S. Kheifets, Angle-dependent time delay in two-color XUV+IR photoemission of he and ne, Phys. Rev. A **96**, 013408 (2017).

[29] F. Morales, T. Bredtmann, and S. Patchkovskii, iSURF: a family of infinite-time surface flux methods, J. Phys. B **49**, 245001 (2016).

[30] A. Maquet and R. Taïeb, Two-colour IR+XUV spectroscopies: the soft-photon approximation, J. Mod. Opt. **54**, 1847 (2007).

[31] D. Toffoli, M. Stener, and P. Decleva, Application of the relativistic time-dependent density functional theory to the photoionization of xenon, J. Phys. B **35**, 1275 (2002).

[32] A. S. Kheifets, Time delay in valence-shell photoionization of noble-gas atoms, Phys. Rev. A **87**, 063404 (2013).

[33] V. K. Dolmatov, Impact of fullerene polarizability on Wigner time delay in photodetachment of fullerene anions C_N^-, J. Phys.: Conf. Ser. **875**, 022013 (2017).